

Boson peak in the dynamical structure factor of network- and packing-type glasses

Hideyuki Mizuno^{1,*} and Emi Minamitani²

¹*Graduate School of Arts and Sciences, The University of Tokyo, Tokyo 153-8902, Japan*

²*SANKEN, University of Osaka, Osaka 567-0047, Japan*

(Dated: January 28, 2026)

Glasses are structurally disordered solids that host, in addition to crystalline-like phonons, vibrational excitations with no direct phononic counterpart. A long-standing universal signature is the excess vibrational density of states (vDOS) over the Debye prediction, known as the boson peak (BP), which has been extensively reported via inelastic neutron and X-ray scattering measurements of the dynamical structure factor $S(q, \omega)$. Here we quantify the vDOS directly from dynamical-structure-factor data and clarify the microscopic origin of the BP. We contrast two routes to extract the vDOS from $S(q, \omega)$: (i) using high-wavenumber q data beyond the Debye wavenumber q_D to access predominantly incoherent scattering and recover the vDOS in a manner analogous to velocity-autocorrelation-based approaches; and (ii) integrating $S(q, \omega)$ over the low- q regime below q_D , which enables a decomposition of the vDOS into contributions from distinct wavenumber sectors and thereby provides direct access to the spatial character of vibrational modes. Focusing on the second route, we demonstrate that the BP in the vDOS emerges as the spectral consequence of a dispersionless excitation band in $S(q, \omega)$. Our main results are obtained from molecular-dynamics simulations, and we further show that the same mechanism is captured by an effective-medium theory for random spring networks, providing a unified interpretation that connects the excess vDOS to the wavenumber-resolved structure of vibrational excitations in glasses.

I. INTRODUCTION

Glasses are structurally disordered solids that, in addition to crystalline-like phonons, support vibrational excitations with no direct phononic counterpart. A central and remarkably universal manifestation is the excess vibrational density of states (vDOS) over the Debye prediction—the boson peak (BP)—observed across a wide range of glasses [1, 2]. Although the BP has been documented for decades, its microscopic origin remains actively debated, in part because experiments do not always access the “bare” vDOS $g(\omega)$ directly (with ω the angular frequency) but instead probe response functions with nontrivial matrix elements—most prominently the dynamical structure factor $S(q, \omega)$, as discussed below. A key goal is therefore to connect the excess vDOS to experimentally accessible observables and to clarify how it is encoded in these measurements.

Experimental access to the vDOS differs sharply between colloidal glasses and atomic/molecular glasses. In colloids, particle coordinates can be tracked directly by confocal or video microscopy, providing an almost first-principles route to vibrational modes. From measured displacement fields one constructs the covariance matrix, from which an effective stiffness (Hessian-like) operator can be inferred, so that the normal modes and $g(\omega)$ can be obtained from its eigenvectors and eigenvalues [3–5]. This approach parallels standard molecular-dynamics (MD) simulations, where the vibrational spectrum is obtained by diagonalizing the $T = 0$ Hessian (dynamical matrix) [6]. Using this experimental framework, low-

frequency excess modes have been investigated as functions of control parameters such as the volume fraction and the coordination number [7, 8].

In atomic and molecular glasses, by contrast, the vDOS is typically accessed indirectly through scattering and spectroscopic probes with nontrivial matrix elements [9–23]. Inelastic neutron scattering (INS) measures the dynamical structure factor $S(q, \omega)$ and provides the most direct experimental route to the vDOS, although in practice it is commonly discussed in terms of a generalized (neutron-weighted) vDOS. Inelastic X-ray scattering (IXS) also measures $S(q, \omega)$ and, by probing primarily longitudinal density fluctuations, constrains the physics behind the vDOS by mapping acoustic dispersions $\omega(q)$ and linewidths (dampings) $\Gamma(q)$, thereby linking the BP regime to the strong damping of acoustic excitations and Ioffe–Regel–like crossovers. Optical probes access different correlation functions (typically at $q \simeq 0$) and thus provide coupling-weighted spectra: for Stokes Raman scattering one often writes $I_R(\omega) = C_R(\omega) [n(\omega) + 1] g(\omega)/\omega$ [24–26], where $n(\omega)$ is the Bose–Einstein occupation factor, while infrared absorption is frequently expressed schematically as $\alpha(\omega) = C_{\text{IR}}(\omega) g(\omega)$ [27–29]. In both cases, extracting $g(\omega)$ requires modeling the coupling functions $C_R(\omega)$ or $C_{\text{IR}}(\omega)$. THz spectroscopy offers complementary information on the same low-frequency optical response in the BP range [30–32].

Motivated by this experimental situation, we focus on routes that connect the BP anomaly in $g(\omega)$ directly to the dynamical structure factor $S(q, \omega)$, the central experimental observable in INS and IXS. Broadly, there are two complementary strategies to infer $g(\omega)$ from $S(q, \omega)$. The first exploits the high-wavenumber regime $q > q_D$, where q_D is the Debye wavenumber, in which incoherent contributions dominate and $S(q, \omega)$ becomes effec-

* hideyuki.mizuno@phys.c.u-tokyo.ac.jp

tively single-particle-like, enabling the reconstruction of $g(\omega)$ [33–36]. This strategy closely parallels the standard estimate based on the Fourier transform of the velocity autocorrelation function, widely used in MD simulations [37, 38]. The second integrates $S(q, \omega)$ over the low- q regime $q < q_D$ to obtain $g(\omega)$ while retaining a decomposition into distinct wavenumber sectors, thereby providing a wavenumber-resolved link between the measured $S(q, \omega)$ and the spatial character of vibrational excitations and their contributions to the BP [39–44].

In the present work, we quantify the vDOS $g(\omega)$ from $S(q, \omega)$ using two complementary routes. The first route uses high- q spectra to provide an accurate and experimentally convenient estimate of $g(\omega)$. Building on the second, wavenumber-resolved route, we show that the BP anomaly in $g(\omega)$ emerges as the spectral consequence of a nearly dispersionless excitation band in $S(q, \omega)$. Our main results are obtained from MD simulations, and we further show that the same interpretation is captured by an effective-medium theory (EMT) for random spring networks [40, 42]. This perspective provides an experimentally grounded bridge between BP phenomenology and the physics of non-phononic excitations in disordered solids.

II. SYSTEM DESCRIPTIONS

In this study, we use MD simulations to analyze three representative glass formers: silica glass as a prototypical covalent network glass, and two packing-dominated (van der Waals) glasses, namely a one-component Lennard–Jones (LJ) glass and a binary soft-sphere (SS) glass. By contrasting network-type and packing-type systems, we aim to assess the universality of the connection between the BP and a dispersionless excitation band.

A. Silica glass

We consider a three-dimensional model of silica (SiO_2) glass composed of N_{Si} silicon atoms and N_{O} oxygen atoms, with the stoichiometric constraint $N_{\text{O}} = 2N_{\text{Si}}$ and total atom number $N = N_{\text{Si}} + N_{\text{O}} = 3N_{\text{Si}}$. The atomic masses are denoted by m_{Si} and m_{O} , with $m_{\text{Si}}/m_{\text{O}} = 1.755$.

Interatomic interactions are modeled using the BKS family of pair potentials, originally introduced in Ref. [45] and subsequently refined in several works [46–50]. In the present study, we employ the SHIK parameterization [50], which has been benchmarked against experiments and first-principles simulations and shown to reproduce thermodynamic properties, structural observables (radial distribution functions, static structure factors, and bond-angle distributions), and elastic moduli. Related BKS-type simulations have examined the mechanical response and vibrational properties of silica

TABLE I. Parameters for the potential of silica glass. $q_{\text{Si}} = 1.7755 e$, $q_{\text{O}} = -q_{\text{Si}}/2$, $r_{cS} = 8.0 \text{ \AA}$, $r_{cL} = 10.0 \text{ \AA}$, and $\gamma_S = \gamma_L = 0.2 \text{ \AA}$.

$\alpha\text{-}\beta$	$A_{\alpha\beta}$ (eV)	$B_{\alpha\beta}$ (\AA^{-1})	$C_{\alpha\beta}$ (eV \AA^6)	$D_{\alpha\beta}$ (eV \AA^{24})
Si–O	23107.8	5.098	139.7	66.0
O–O	1120.5	2.893	26.1	16800.0
Si–Si	2797.9	4.407	0.0	3423204.0

glasses [51–53], and the effects of densification on the BP have also been reported recently [54].

The total interaction is written as the sum of a short-range part $v_S(r)$ and a Coulomb part $v_L(r)$. The short-range contribution reads

$$v_S(r) = A_{\alpha\beta} \exp(-B_{\alpha\beta}r) - \frac{C_{\alpha\beta}}{r^6} + \frac{D_{\alpha\beta}}{r^{24}}, \quad (1)$$

where r is the interparticle distance and $\alpha, \beta \in \{\text{Si}, \text{O}\}$. The parameters $A_{\alpha\beta}$, $B_{\alpha\beta}$, $C_{\alpha\beta}$, and $D_{\alpha\beta}$ are listed in Table I. The Coulomb term is

$$v_L(r) = \frac{q_\alpha q_\beta}{r}, \quad (2)$$

with partial charges $q_{\text{Si}} = 1.7755 e$ and $q_{\text{O}} = -q_{\text{Si}}/2$, ensuring overall charge neutrality (here e is the elementary charge).

We apply cutoffs $r_{cS} = 8.0 \text{ \AA}$ and $r_{cL} = 10.0 \text{ \AA}$ to $v_S(r)$ and $v_L(r)$, respectively. For the Coulomb interaction, this cutoff is referred to as Wolf truncation [46, 47]. To avoid discontinuities at the cutoffs, both contributions are smoothed according to

$$\begin{aligned} \phi_S(r) &= [v_S(r) - v_S(r_{cS}) - (r - r_{cS})v'_S(r_{cS})]G_{cS}(r), \\ \phi_L(r) &= [v_L(r) - v_L(r_{cL})]G_{cL}(r), \end{aligned} \quad (3)$$

with

$$\begin{aligned} G_{cS}(r) &= \exp\left[-\frac{\gamma_S^2}{(r - r_{cS})^2}\right], \\ G_{cL}(r) &= \exp\left[-\frac{\gamma_L^2}{(r - r_{cL})^2}\right], \end{aligned} \quad (4)$$

where $\gamma_S = \gamma_L = 0.2 \text{ \AA}$.

We note that BKS-type models are pairwise additive, comprising a short-range two-body term together with a long-range Coulomb contribution, and therefore do not explicitly include angular many-body interactions that encode covalent directionality. More explicit descriptions of covalent bonding incorporate angular forces, notably the Vashishta potential [55], which adds three-body interactions associated with O–Si–O and Si–O–Si angles. Nevertheless, BKS-type models implicitly capture key aspects of covalent directionality through their parameterization and have been shown to reproduce, with quantitative accuracy, the thermodynamic properties, structural observables, and elastic moduli of silica glass [45–50].

We carried out three independent MD simulations using LAMMPS [56]. The mass density was fixed at

$\rho = 2.20 \text{ g/cm}^3$, and the temperature was controlled using a Nosé–Hoover thermostat [57, 58]. Starting from randomized Si and O positions, we equilibrated the system at $T = 3500 \text{ K}$ for 100 ps to obtain a homogeneous liquid. We then quenched to $T = 300 \text{ K}$ at a rate of 1 K/ps and equilibrated at $T = 300 \text{ K}$ for an additional 100 ps. Finally, atomic velocities were set to zero and the configuration was energy-minimized to obtain the inherent structure $\vec{r} = [\vec{r}_1, \vec{r}_2, \dots, \vec{r}_N]$.

To cover a wide range of wavenumbers q and frequencies ω , we considered multiple system sizes from $N = 1.5 \times 10^4$ up to 2.4×10^5 atoms. All reported results are averages over the three independent inherent structures.

B. Lennard–Jones glass

As a simple packing-type atomic glass, we consider a three-dimensional one-component LJ system that has been studied extensively in previous works [59–61]. Particles interact via

$$v(r) = 4\epsilon \left[\left(\frac{\sigma}{r} \right)^{12} - \left(\frac{\sigma}{r} \right)^6 \right], \quad (5)$$

where r is the interparticle distance and σ sets the particle diameter. The potential is truncated at $r_c = 2.5\sigma$. To suppress artifacts associated with the cutoff discontinuity [62], we employ the shifted-force form

$$\phi(r) = v(r) - v(r_c) - (r - r_c)v'(r_c), \quad (6)$$

which makes both $\phi(r)$ and its derivative vanish at $r = r_c$. All particles have equal mass m , and we use reduced LJ units with length σ , mass m , and energy ϵ . The number density is $\hat{\rho} = N/V = 1.015$, where V is the system volume, and the system size ranges from $N = 1.6 \times 10^4$ to 1.024×10^6 .

C. Soft-sphere glass

We further study a three-dimensional binary SS mixture analyzed in our previous works [63–65]. Particles of types $\alpha, \beta \in \{L, S\}$ interact through a 12-inverse-power-law potential

$$v(r) = \epsilon \left(\frac{\sigma_{\alpha\beta}}{r} \right)^{12}, \quad (7)$$

where $\sigma_{\alpha\beta} = (\sigma_\alpha + \sigma_\beta)/2$. The size ratio is $\sigma_S/\sigma_L = 0.7$, and we take an equimolar composition $x_{L,S} = N_{L,S}/N = 1/2$ with $N = N_L + N_S$. As for the LJ system, we use the smoothed interaction $\phi(r)$ in Eq. (6). All particles have the same mass m , and we define the length unit as $\sigma = \left(\sum_{\alpha,\beta=L,S} x_\alpha x_\beta \sigma_{\alpha\beta}^3 \right)^{1/3}$. The number density is again $\hat{\rho} = N/V = 1.015$, and we consider system sizes from $N = 1.6 \times 10^4$ to 1.024×10^6 .

III. NUMERICAL ANALYSES

A. Vibrational modes

For each inherent structure $\vec{r} = [\vec{r}_1, \vec{r}_2, \dots, \vec{r}_N]$, we perform a standard normal-mode analysis based on the $3N \times 3N$ dynamical matrix. Solving the corresponding eigenvalue problem yields eigenvalues $\{\lambda_k\}$ and eigenvectors $\{\vec{e}_k = [\vec{e}_{k,1}, \vec{e}_{k,2}, \dots, \vec{e}_{k,N}]\}$ for $k = 1, 2, \dots, 3N$ [6]. The eigenfrequencies are $\omega_k = \sqrt{\lambda_k}$, and the eigenvectors are normalized as $\vec{e}_k \cdot \vec{e}_l = \sum_{i=1}^N \vec{e}_{k,i} \cdot \vec{e}_{l,i} = \delta_{k,l}$, where $\delta_{k,l}$ is the Kronecker delta. In the following analyses based on the mode data $\{\omega_k, \vec{e}_k\}$, we discard the three translational zero modes.

To access both moderate and very low frequencies, we combine results across multiple system sizes, following the strategy of Ref. [66]. We compute all modes for the smallest system, whereas for larger systems we obtain only low-frequency modes. We then merge the mode datasets as a function of ω_k ; spectra from different sizes overlap and match smoothly, extending the accessible frequency window toward lower ω . The vDOS $g(\omega)$ in Eq. (8) and the dynamical structure factors $S_\alpha(q, \omega)$ in Eq. (11) are evaluated from these combined datasets, and data from different sizes are presented together.

B. Vibrational density of states

Given the eigenfrequencies $\{\omega_k\}$, the vDOS is computed as

$$g(\omega) = \frac{1}{3N} \sum_{k=1}^{3N} \delta(\omega - \omega_k), \quad (8)$$

where δ is the Dirac delta function.

In an isotropic elastic continuum, low-frequency excitations are phonons with linear dispersions $\omega = c_T q$ and $\omega = c_L q$, where c_T and c_L are the transverse and longitudinal sound speeds, respectively [67]. Counting phonon states leads to the Debye prediction,

$$g_D(\omega) = A_D \omega^2 = \frac{3}{\omega_D^3} \omega^2 \propto \omega^2, \quad (9)$$

where $A_D = 3/\omega_D^3$ is the Debye level and ω_D is the Debye frequency, given by

$$\omega_D = \left(\frac{c_L^{-3} + 2c_T^{-3}}{3} \right)^{-1/3} q_D = \left(\frac{18\pi^2 \hat{\rho}}{c_L^{-3} + 2c_T^{-3}} \right)^{1/3}, \quad (10)$$

with the Debye wavenumber $q_D = (6\pi^2 \hat{\rho})^{1/3}$. The resulting values of c_L , c_T , q_D , A_D , and ω_D for each model glass are summarized in Table II.

TABLE II. Physical quantities including elastic moduli and Debye values. For silica glass, the quantities are given as the mass density ρ (g/cm³), elastic moduli K and G (GPa), sound speeds c_L and c_T (m/s), wavenumber q (Å⁻¹), Debye level A_D (THz⁻³), and frequency ω (THz). Note that ν denotes the Poisson ratio.

Glass	ρ	K	K_A	K_N	$\frac{K_N}{K_A}$ (%)	G	G_A	G_N	$\frac{G_N}{G_A}$ (%)	ν	c_L	c_T	$\frac{c_L}{c_T}$	q_D	A_D	ω_D	ω_{BP}
Silica	2.20	40.9	172	131	76.3	30.5	104	73.6	73.7	0.202	6090	3720	1.64	1.58	0.00257	10.5	1.21
LJ	1.015	61.2	61.7	0.530	0.859	13.6	35.8	22.2	61.9	0.396	8.84	3.67	2.41	3.92	0.000699	16.3	1.05
SS	1.015	40.8	40.8	0.00	0.00	6.21	14.7	8.50	57.8	0.428	6.96	2.47	2.81	3.92	0.00225	11.0	0.798

C. Elastic moduli

We compute the elastic moduli—the bulk modulus K and the shear modulus G —within the harmonic (athermal) linear-response framework [6, 68, 69]. These moduli determine the longitudinal and transverse sound speeds, and thereby the Debye quantities used throughout this work, including the Debye frequency ω_D and the Debye level A_D .

Table II summarizes K , G , and the derived Debye parameters for the three model glasses studied here (silica, LJ, and SS). In amorphous solids, elastic deformation generally contains both affine and nonaffine components [60, 68–70], such that an elastic modulus can be decomposed as $M = M_A - M_N$, where M_A and M_N denote the affine and nonaffine contributions, respectively. We also report in Table II the Poisson ratio $\nu = (3K - 2G)/(6K + 2G)$, which is approximately $\nu \simeq 0.2$ for silica glass, compared with $\nu \simeq 0.4$ for LJ and SS glasses. Following the empirical correlation discussed in Refs. [71, 72], values near $\nu \approx 0.2$ are characteristic of “strong” glasses, whereas $\nu \approx 0.4$ is typical of “fragile” glasses.

D. Dynamical structure factor

Using the mode-resolved information $\{\omega_k, \vec{e}_k\}$, we compute the dynamical structure factors $S_\alpha(q, \omega)$, with $\alpha \in \{T, L\}$ labeling transverse ($\alpha = T$) and longitudinal ($\alpha = L$) components, following Refs. [6, 73]:

$$S_\alpha(q, \omega) = \frac{k_B T}{2N} \frac{q^2}{\omega^2} \sum_{k=1}^{3N} F_{k,\alpha}(q) \delta(\omega - \omega_k), \quad (11)$$

where

$$F_{k,T}(q) = \left| \sum_{i=1}^N \left(\frac{\vec{e}_{k,i}}{\sqrt{m_i}} \times \hat{q} \right) \exp(i\vec{q} \cdot \vec{r}_i) \right|^2, \quad (12)$$

$$F_{k,L}(q) = \left| \sum_{i=1}^N \left(\frac{\vec{e}_{k,i}}{\sqrt{m_i}} \cdot \hat{q} \right) \exp(i\vec{q} \cdot \vec{r}_i) \right|^2.$$

Here k_B is the Boltzmann constant, \vec{q} is the wavevector, $q = |\vec{q}|$, and $\hat{q} = \vec{q}/q$. Scattering experiments predomi-

nantly access the longitudinal component $S_L(q, \omega)$ [74].

1. Incoherent-scattering route to the vDOS

As described in the Introduction, a practical route to estimate the vDOS from scattering observables is to use the large-wavenumber regime $q > q_D$, where the measured spectrum becomes effectively single-particle-like and can be related to $g(\omega)$ within an incoherent-scattering approximation. Focusing on the longitudinal dynamical structure factor, which is the component most directly accessed in scattering experiments [74], $S_L(q, \omega)$ can be approximated within an incoherent-scattering (self) approximation as

$$\begin{aligned} S_L(q, \omega) &\approx \frac{k_B T}{2N} \frac{q^2}{\omega^2} \sum_{k=1}^{3N} \sum_{i=1}^N \left(\frac{\vec{e}_{k,i}}{\sqrt{m_i}} \cdot \hat{q} \right)^2 \delta(\omega - \omega_k), \\ &\approx \frac{k_B T}{2N} \frac{q^2}{\omega^2} \sum_{k=1}^{3N} \sum_{i=1}^N \frac{|\vec{e}_{k,i}|^2}{3m_i} \delta(\omega - \omega_k), \\ &\approx \frac{k_B T}{2} \frac{q^2}{\omega^2} M(\omega)^{-1} g(\omega), \end{aligned} \quad (13)$$

where we used the angular average over the direction of \hat{q} , $\langle (\vec{a} \cdot \hat{q})^2 \rangle_{\hat{q}} = |\vec{a}|^2/3$, in the second line. The effective mass is defined through $M^{-1} = \sum_{i=1}^N |\vec{e}_{k,i}|^2/m_i$ evaluated at $\omega = \omega_k$; thus $M(\omega)$ is mode dependent and therefore frequency dependent. This $M(\omega)$ accounts for the mass weighting of eigenmodes in multi-component systems. For one-component systems, $M(\omega)$ reduces to the particle mass, $M(\omega) = m$. We then obtain

$$g_{\text{inc}}(\omega) = 2M(\omega)\omega^2 \frac{S_L(q, \omega)}{q^2 k_B T}. \quad (14)$$

An analogous derivation for the transverse channel $S_T(q, \omega)$ yields

$$g_{\text{inc}}(\omega) = M(\omega)\omega^2 \frac{S_T(q, \omega)}{q^2 k_B T}. \quad (15)$$

In practice, to improve the accuracy of the incoherent-scattering approximation, we compute $g_{\text{inc}}(\omega)$ by averaging the right-hand side of Eq. (14) over a high- q window

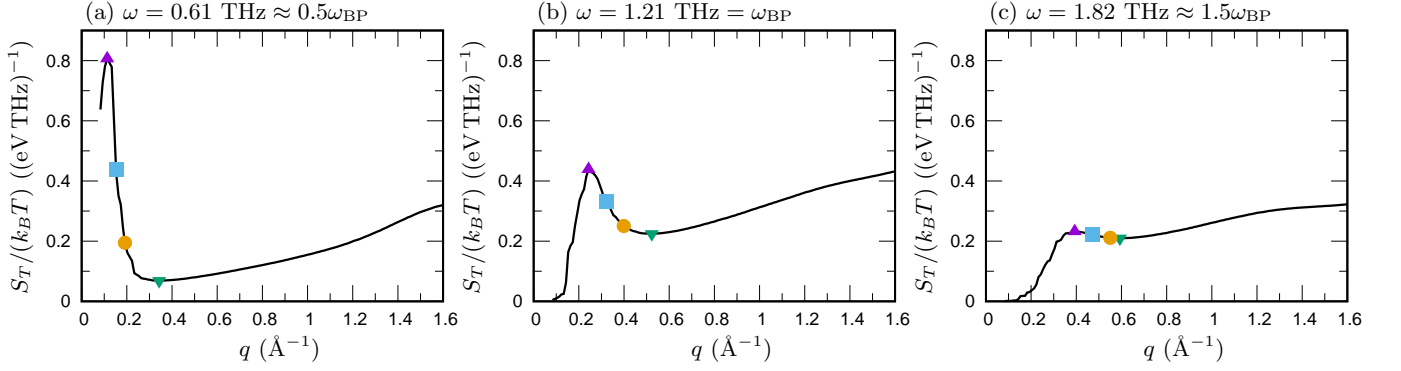


FIG. 1. Crossover wavenumber $q_T(\omega)$ between phononic and non-phononic excitations in silica glass. The transverse dynamical structure factor $S_T(q, \omega)/(k_B T)$ is plotted as a function of wavenumber q for three representative frequencies: (a) $\omega = 0.61$ THz $\approx 0.5\omega_{BP}$, (b) $\omega = 1.21$ THz $= \omega_{BP}$, and (c) $\omega = 1.82$ THz $\approx 1.5\omega_{BP}$. Orange circles indicate $q_T(\omega)$ for each frequency. Purple upward triangles and green downward triangles mark the wavenumbers q_{\max} and q_{\min} at which $S_T(q, \omega)$ takes its local maximum S_{\max} and local minimum S_{\min} , respectively. The cyan squares indicate the wavenumber $q_{\max} + q_{\text{half}}$, where q_{half} is defined as the half-width measured from the phonon-branch peak such that $S_T(q, \omega)$ has decreased from S_{\max} by half the peak-to-trough amplitude, $(S_{\max} - S_{\min})/2$. The crossover wavenumber is then defined as $q_T(\omega) = q_{\max} + 2q_{\text{half}}$, and is shown by the orange circles.

$q_1 \leq q \leq q_2$ [33–36], which corresponds to Eq. (22). This high- q strategy exploits scattering dominated by essentially single-particle vibrations and thus provides a reconstruction of the vDOS in close analogy with the standard estimate based on the Fourier transform of the velocity autocorrelation function [37, 38].

2. Wavenumber-resolved route to the vDOS

As a second route, we access the vDOS by integrating the low- q regime $q < q_D$, as outlined below. Integrating Eqs. (11)–(12) over $q \in [0, q_D]$ gives

$$\begin{aligned} & \int_0^{q_D} \left\{ \frac{S_T(q, \omega)}{k_B T} + \frac{S_L(q, \omega)}{k_B T} \right\} dq \\ &= \frac{1}{2N\omega^2} \sum_{k=1}^{3N} \delta(\omega - \omega_k) \left(\sum_{i,j=1}^N \frac{\vec{e}_{k,i} \cdot \vec{e}_{k,j}}{\sqrt{m_i m_j}} \int_0^{q_D} e^{i\vec{q} \cdot (\vec{r}_i - \vec{r}_j)} q^2 dq \right) \end{aligned} \quad (16)$$

We now apply an isotropic-medium approximation. In an isotropic elastic continuum, the eigenmodes are plane-wave elastic excitations,

$$\vec{e}_{k,i} \propto \vec{s}_\alpha e^{i\vec{q} \cdot \vec{r}_i}, \quad (17)$$

where $\alpha \in \{T, L\}$ labels transverse ($\alpha = T$) and longitudinal ($\alpha = L$) polarizations, and \vec{s}_α is the corresponding polarization unit vector [6]. Plane waves with wavevectors restricted to $0 \leq |\vec{q}| \leq q_D$ form an orthogonal and complete basis within the Debye cutoff. Accordingly, one may use the completeness relation

$$\sum_{\substack{\vec{q}: 0 \leq |\vec{q}| \leq q_D \\ \alpha \in \{T, L\}}} (\vec{s}_\alpha e^{i\vec{q} \cdot \vec{r}_i}) \cdot (\vec{s}_\alpha^* e^{-i\vec{q} \cdot \vec{r}_j}) = \sum_{\vec{q}: 0 \leq |\vec{q}| \leq q_D} e^{i\vec{q} \cdot (\vec{r}_i - \vec{r}_j)} \propto \delta_{i,j} \quad (18)$$

where $*$ denotes complex conjugation and we used $\sum_{\alpha \in \{T, L\}} \vec{s}_\alpha \cdot \vec{s}_\alpha^* = 1$ [6]. Under this isotropic-medium approximation [Eq. (18)], the q -integral in Eq. (16) simplifies to

$$\begin{aligned} & \int_0^{q_D} e^{i\vec{q} \cdot (\vec{r}_i - \vec{r}_j)} q^2 dq = \frac{1}{4\pi} \int_{0 \leq |\vec{q}| \leq q_D} e^{i\vec{q} \cdot (\vec{r}_i - \vec{r}_j)} d^3 \vec{q} \\ &= \frac{1}{4\pi} \delta_{i,j} \left(\int_{0 \leq |\vec{q}| \leq q_D} d^3 \vec{q} \right) = \frac{q_D^3}{3} \delta_{i,j}. \end{aligned} \quad (19)$$

Substituting Eq. (19) into Eq. (16) yields

$$\begin{aligned} & \int_0^{q_D} \left\{ \frac{S_T(q, \omega)}{k_B T} + \frac{S_L(q, \omega)}{k_B T} \right\} dq \\ & \approx \frac{q_D^3}{2\omega^2} \frac{1}{3N} \sum_{k=1}^{3N} \delta(\omega - \omega_k) \left(\sum_{i=1}^N \frac{|\vec{e}_{k,i}|^2}{m_i} \right) = \frac{q_D^3}{2M(\omega)} \frac{g(\omega)}{\omega^2}, \end{aligned} \quad (20)$$

where $M(\omega)$ is the effective mass defined in Eq. (13). We then obtain

$$\frac{g_{T+L}(\omega)}{\omega^2} = \frac{2M(\omega)}{q_D^3} \int_0^{q_D} \left[\frac{S_T(q, \omega)}{k_B T} + \frac{S_L(q, \omega)}{k_B T} \right] dq, \quad (21)$$

which corresponds to Eq. (23).

In theoretical treatments [39–44], Eq. (21) is used to evaluate the vDOS from the dynamical structure factor (or, equivalently, from the corresponding Green's functions). A key advantage of this low- q route is that it retains a decomposition into distinct wavenumber sectors, thereby providing a wavenumber-resolved link between the measured $S_\alpha(q, \omega)$ and the spatial character of vibrational excitations and their contributions to the BP.

3. Crossover wavenumber $q_T(\omega)$ between phononic and non-phononic excitations

As shown in Fig. 4, the transverse dynamical structure factor $S_T(q, \omega)$ exhibits a phonon branch with an approximately linear dispersion at low q , and a non-phononic, nearly dispersionless band at higher q . In Sec. IV D, Eq. (24) introduces a crossover wavenumber $q_T(\omega)$ to separate, for each frequency ω , the vDOS into phononic and non-phononic contributions. Here we describe how $q_T(\omega)$ is determined in practice.

We determine $q_T(\omega)$ from $S_T(q, \omega)$ viewed as a function of q at fixed ω . Figure 1 plots $S_T(q, \omega)/(k_B T)$ versus q for three representative frequencies, including ω_{BP} as well as frequencies below and above ω_{BP} . Orange circles indicate the resulting $q_T(\omega)$ for each frequency, obtained as follows. (i) We first identify the phonon-branch peak, where $S_T(q, \omega)$ attains a local maximum S_{\max} at wavenumber q_{\max} (purple upward triangles). (ii) We then locate the wavenumber q_{\min} at which $S_T(q, \omega)$ reaches a local minimum S_{\min} after the phonon-branch feature has decayed and the spectrum enters the dispersionless-band regime (green downward triangles). (iii) Next, we determine q_{half} as a half-width measured from q_{\max} such that $S_T(q, \omega)$ at $q = q_{\max} + q_{\text{half}}$ has decreased from S_{\max} by half the peak-to-trough amplitude, *i.e.*, by $(S_{\max} - S_{\min})/2$ (cyan squares). (iv) Finally, we define the crossover wavenumber as $q_T(\omega) = q_{\max} + 2q_{\text{half}}$, shown by the orange circles in Fig. 1.

The resulting $q_T(\omega)$ is shown as the green curve in Fig. 4. Although this construction is not unique, Fig. 4 shows that the resulting $q_T(\omega)$ provides a reasonable and physically motivated boundary between the phonon-branch region and the non-phononic excitations. We therefore adopt this definition throughout the present work.

IV. RESULTS

A. Dynamical structure factor

Figure 2 shows the simulated dynamical structure factors for the three glasses. The upper panels (a,c,e) display the transverse component $S_T(q, \omega)$, whereas the lower panels (b,d,f) show the longitudinal component $S_L(q, \omega)$. Focusing first on $S_T(q, \omega)$, silica, LJ, and SS glasses all exhibit qualitatively similar dependences on q and ω in the low-frequency regime up to the Debye frequency ω_D . In particular, in the low- ω region around the BP frequency, $S_T(q, \omega)$ displays a linearly dispersing acoustic branch together with an additional, nearly q -independent (dispersionless) excitation band, which we discuss in detail below (see Fig. 4).

The longitudinal channel, however, highlights a marked difference between the network glass (silica) and the packing-dominated glasses (LJ and SS). For silica, $S_L(q, \omega)$ closely mirrors $S_T(q, \omega)$: besides the longitudi-

nal acoustic branch, a dispersionless band is also visible in the low- ω region near the BP frequency. For LJ and SS glasses, by contrast, $S_L(q, \omega)$ differs qualitatively from $S_T(q, \omega)$; the dispersionless band prominent in $S_T(q, \omega)$ is not apparent in $S_L(q, \omega)$, while the longitudinal acoustic branch persists to substantially higher frequencies, up to $\omega \simeq 20$ for LJ and $\omega \simeq 13$ for SS. These observations suggest that transverse and longitudinal excitations are more strongly coupled in silica glass, whereas they are effectively decoupled in LJ and SS glasses.

This transverse-longitudinal coupling/decoupling trend is consistent with the nonaffine character of the elastic response, as summarized in Table II. In packing-dominated LJ and SS glasses, the shear modulus G exhibits a sizable nonaffine reduction (about 60% of the affine contribution), whereas the bulk modulus K remains close to its affine value, with a nonaffine correction of order 1%; thus transverse (shear) and longitudinal (compressional) deformations are affected very differently by nonaffinity. In contrast, in the covalent network glass (silica) both the shear and bulk moduli display strong nonaffine contributions, with nonaffine relaxations substantially reducing the moduli from their affine values and the nonaffine component reaching roughly 75% of the affine one for both moduli. This pronounced nonaffinity is brought about by the absence of local centrosymmetry in tetrahedral network structures [75, 76] and has also been reported for amorphous silicon [77] and noncentrosymmetric crystals such as α -quartz [78]. As a consequence, K and G become closer in magnitude in silica glass than in packing-type glasses.

Taken together, these results indicate that the degree of transverse-longitudinal coupling in $S_\alpha(q, \omega)$ correlates with the extent of nonaffinity in the corresponding elastic moduli. In network glasses, strong nonaffinity in both shear and bulk responses is accompanied by similar transverse and longitudinal spectral features. In packing-dominated glasses, the near-affine bulk response is accompanied by a longitudinal spectrum in which the acoustic branch persists to substantially higher frequencies, with little trace of the transverse dispersionless band.

B. Incoherent-scattering route to the vDOS

As a first route, we access the vDOS from the dynamical structure factor in the large-wavenumber regime. Concretely, we adopt the incoherent-scattering approximation and use the longitudinal component $S_L(q, \omega)$ in a high- q window $q_1 \leq q \leq q_2$ to define [33–36] [see Eq. (14)]

$$g_{\text{inc}}(\omega) = 2M(\omega)\omega^2 \left\{ \frac{1}{q_2 - q_1} \int_{q_1}^{q_2} \frac{S_L(q, \omega)}{q^2 k_B T} dq \right\}. \quad (22)$$

For silica glass, we choose $q_1 = 2.5 \text{ \AA}^{-1}$ and $q_2 = 5.25 \text{ \AA}^{-1}$, both larger than the Debye wavenumber $q_D =$

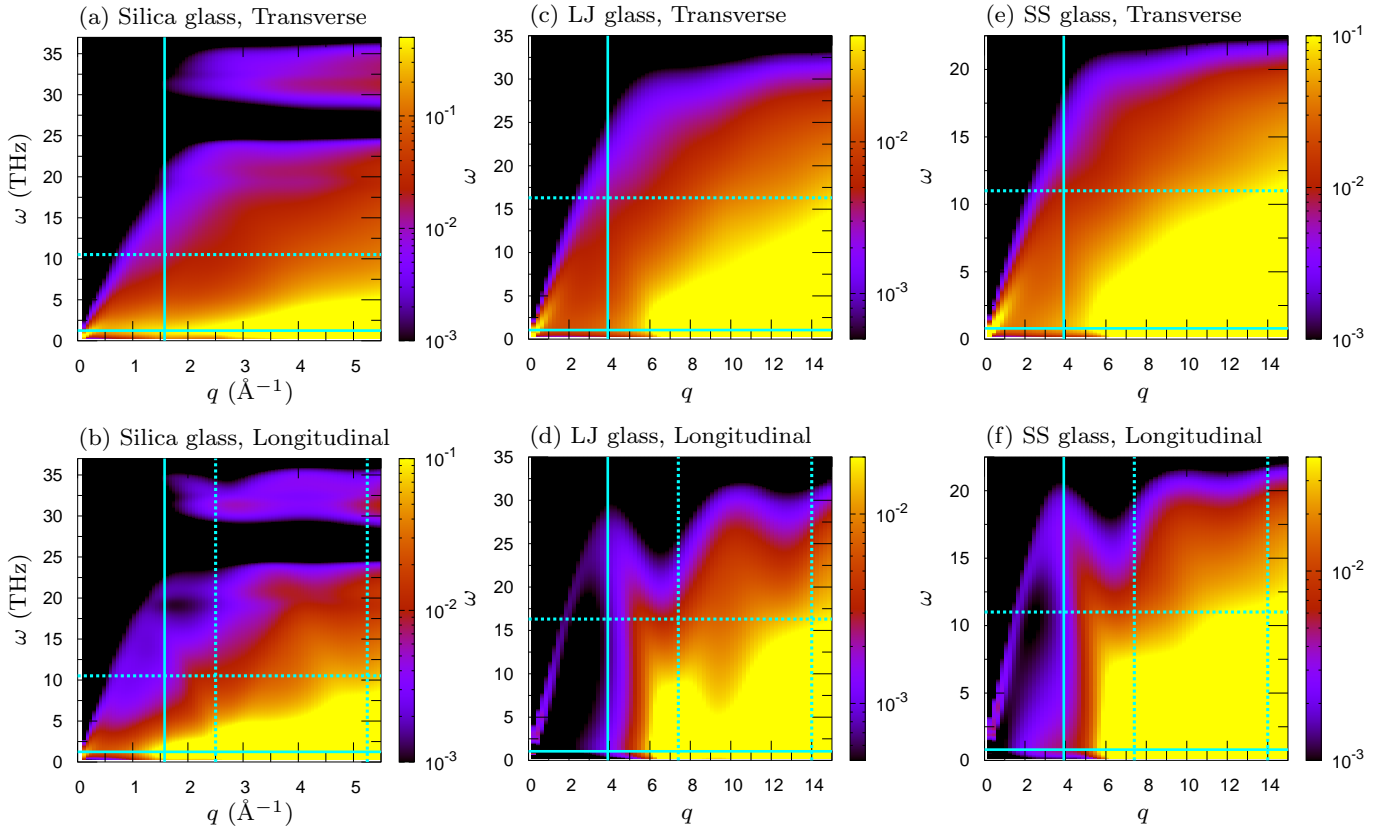


FIG. 2. Dynamical structure factors. (a,b) Silica glass, (c,d) LJ glass, and (e,f) SS glass. The transverse component $S_T(q, \omega)/(k_B T)$ is shown as a function of q and ω in upper panels (a,c,e), and the longitudinal component $S_L(q, \omega)/(k_B T)$ in lower panels (b,d,f). For silica glass, values are reported in units of $(\text{eV THz})^{-1}$. The horizontal solid and dashed lines indicate the BP frequency ω_{BP} and the Debye frequency ω_D , respectively. The vertical solid line marks the Debye wavenumber q_D , while the vertical dashed lines in (b,d,f) mark q_1 and q_2 used to compute $g_{\text{inc}}(\omega)$ in Eq. (22).

1.58 \AA^{-1} , as indicated in Fig. 2(b), so that the analysis is performed well within the large- q regime. For LJ and SS glasses, we likewise select q_1 and q_2 in the regime $q > q_D$; the specific choices are given together with the corresponding datasets in Fig. 2(d,f).

Figure 3 compares $g_{\text{inc}}(\omega)$ obtained from Eq. (22) (purple curve) with the exact vDOS $g(\omega)$ computed from the full set of eigenfrequencies via Eq. (8) (black curve). In the lower panels [Fig. 3(b,d,f)], we emphasize the low-frequency regime by plotting the reduced vDOS $g(\omega)/\omega^2$, which highlights the BP anomaly. We find that $g_{\text{inc}}(\omega)$ faithfully reproduces $g(\omega)$ over the full frequency range, including the BP feature and its characteristic frequency ω_{BP} . These results validate the large- q /incoherent-scattering route as a reliable procedure for extracting $g(\omega)$ from $S_L(q, \omega)$.

A further practical advantage is that scattering experiments predominantly probe the longitudinal channel $S_L(q, \omega)$ and often yield especially robust statistics in the large- q regime. Accordingly, Eq. (22) provides a convenient experimental pathway to estimate $g(\omega)$ directly from high- q measurements of $S_L(q, \omega)$.

C. Wavenumber-resolved route to the vDOS

Next, we focus on the second, wavenumber-resolved route to the vDOS. In this approach, $g(\omega)$ is estimated by integrating the dynamical structure factor over wavenumbers from 0 to q_D . Specifically, we use [see Eq. (21)]

$$\begin{aligned} \frac{g_{T+L}(\omega)}{\omega^2} &= \frac{2M(\omega)}{q_D^3} \int_0^{q_D} \left[\frac{S_T(q, \omega)}{k_B T} + \frac{S_L(q, \omega)}{k_B T} \right] dq, \\ &\equiv \frac{g_T(\omega)}{\omega^2} + \frac{g_L(\omega)}{\omega^2}. \end{aligned} \quad (23)$$

This expression naturally decomposes the vDOS into transverse and longitudinal contributions, $g_T(\omega)$ and $g_L(\omega)$, defined by integrating $S_T(q, \omega)$ and $S_L(q, \omega)$ over $0 < q < q_D$, respectively. In theoretical treatments [39–44], Eq. (23) is commonly used to evaluate the vDOS from the dynamical structure factor (or, equivalently, from the corresponding Green’s functions).

Figure 3 shows the transverse $g_T(\omega)$ and longitudinal $g_L(\omega)$, together with their sum $g_{T+L}(\omega) \equiv g_T(\omega) + g_L(\omega)$ [79]. For silica glass [panels (a,b)], $g_{T+L}(\omega)$ captures the overall ω dependence of the exact vDOS $g(\omega)$, al-

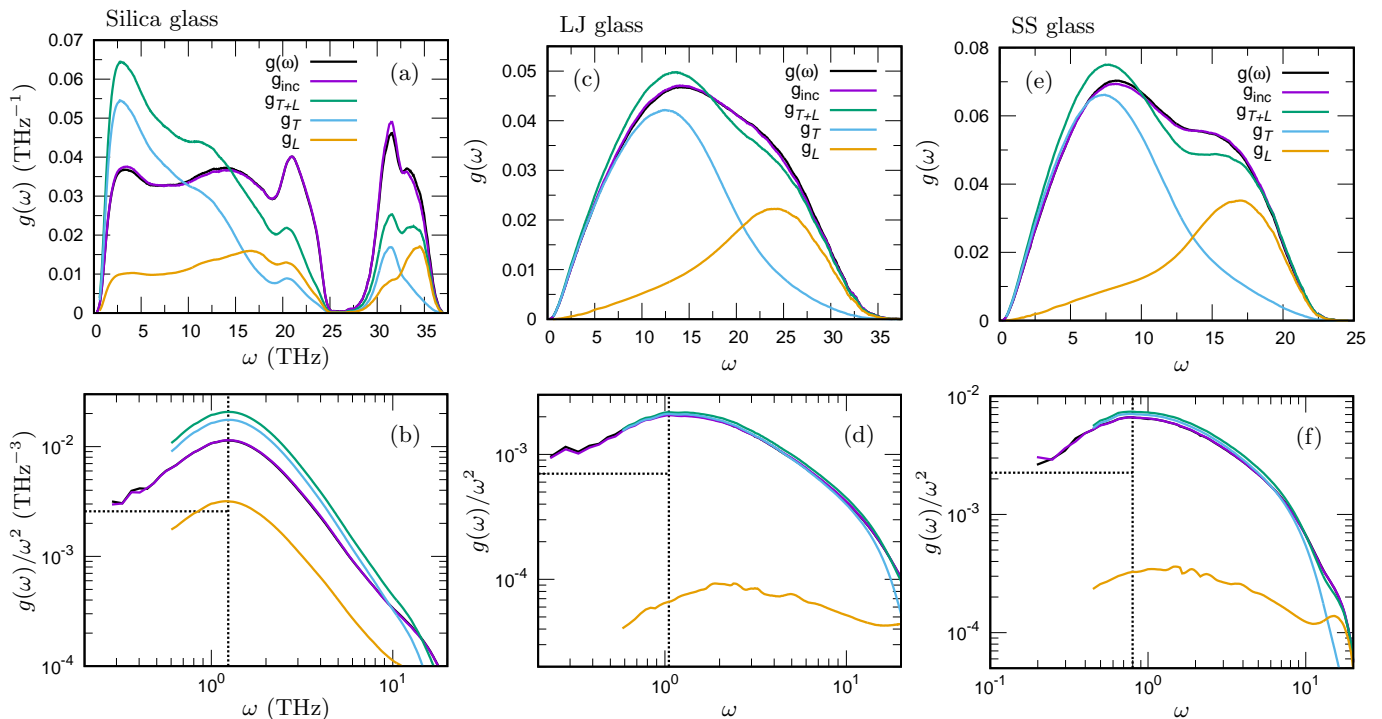


FIG. 3. Vibrational density of states. (a,b) Silica glass, (c,d) LJ glass, and (e,f) SS glass. $g(\omega)$ and $g(\omega)/\omega^2$ (black) are shown as functions of frequency ω , together with $g_{\text{inc}}(\omega)$ (purple), calculated from $S_L(q, \omega)$ over the high-wavenumber range $q_1 \leq q \leq q_2$ (with $q_1, q_2 > q_D$) using Eq. (22). Also shown are the transverse and longitudinal components $g_T(\omega)$ (cyan) and $g_L(\omega)$ (orange), obtained by integrating $S_T(q, \omega)$ and $S_L(q, \omega)$ over $q \leq q_D$ as in Eq. (23), and their sum $g_{T+L}(\omega) = g_T(\omega) + g_L(\omega)$ (green). The vertical and horizontal dotted lines in (b,d,f) indicate the BP frequency ω_{BP} and the Debye level A_D , respectively.

though noticeable quantitative deviations remain. For the packing-dominated glasses, Eq. (23) performs better: as shown in panels (c–f), $g_{T+L}(\omega)$ quantitatively reproduces $g(\omega)$ for the LJ and SS glasses. The larger deviations in silica glass are plausibly attributed to its tetrahedral network topology, in contrast to the more randomly and tightly packed structures of the LJ and SS glasses, which may lead to departures from the isotropic-medium approximation [Eq. (18)] and hence from Eq. (23). Nevertheless, even for silica glass the estimate $g_{T+L}(\omega)$ from Eq. (23) captures the overall frequency dependence of the exact $g(\omega)$; in particular, in the BP regime it reproduces the characteristic ω dependence, including the BP frequency ω_{BP} . This indicates that Eq. (23) provides a useful basis for vDOS analysis within the present wavenumber-resolved route.

A further key observation in Fig. 3(b,d,f) is that, in the low- ω region around ω_{BP} , the transverse contribution $g_T(\omega)$ substantially exceeds the longitudinal contribution $g_L(\omega)$ in all glasses studied here (compare the cyan and orange curves). This indicates that the BP is predominantly associated with transverse vibrational states. Such transverse dominance has been reported previously for packing-type glasses [44, 59, 63, 64] and also for network-type systems such as amorphous silicon [80–82].

Importantly, however, silica glass differs from the

packing-dominated LJ and SS glasses in the relative weight of the longitudinal sector. Notably, in silica glass, $g_L(\omega)$ is larger and closer to $g_T(\omega)$ than in the LJ and SS glasses, tracking the ω dependence of the exact $g(\omega)$ more faithfully, including the location of ω_{BP} [panel (b)]. By contrast, this behavior is not observed for the LJ and SS glasses, where $g_L(\omega)$ remains much smaller than $g_T(\omega)$ in the BP regime. This distinction mirrors the dynamical-structure-factor phenomenology in Fig. 2: in silica glass, the transverse and longitudinal channels exhibit similar low- q /low- ω spectral features (indicative of stronger transverse–longitudinal coupling), whereas in the LJ and SS glasses, the longitudinal spectrum shows a pronounced acoustic branch that persists to substantially higher frequencies, with little trace of the transverse dispersionless band (indicative of effective decoupling).

D. Phononic and non-phononic components of the vDOS

The key advantage of the second, wavenumber-resolved route to the vDOS is that it enables a quantitative decomposition of how each wavenumber sector of $S_T(q, \omega)$ and $S_L(q, \omega)$ contributes to the vDOS $g(\omega)$. Exploiting this capability, we decompose the vDOS into contributions from the phonon branch and from the remaining

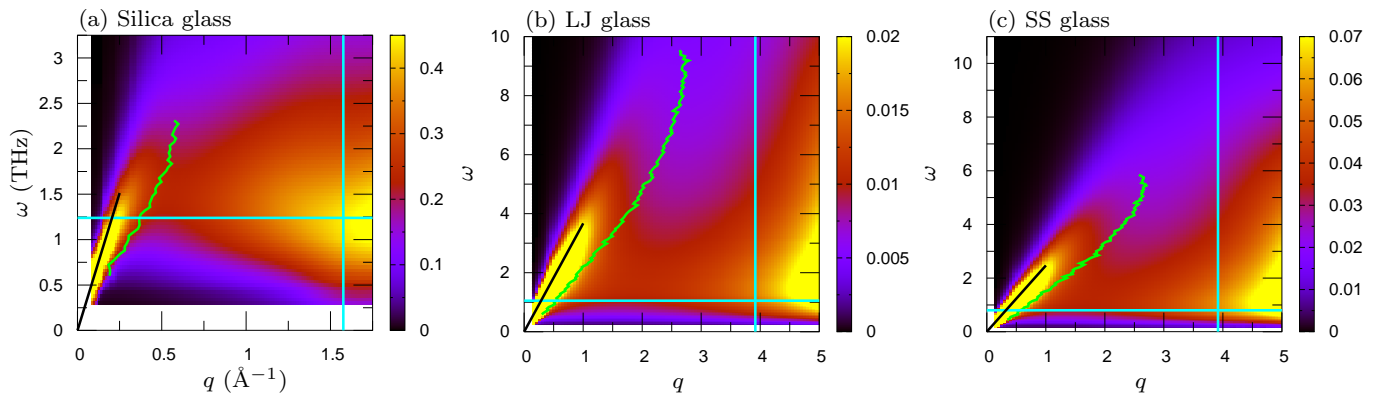


FIG. 4. Transverse dynamical structure factor at low wavenumbers and low frequencies. (a) Silica glass, (b) LJ glass, and (c) SS glass. $S_T(q, \omega)/(k_B T)$ is shown as a function of q and ω . For silica glass, values are reported in units of $(\text{eV THz})^{-1}$. The vertical line marks the Debye wavenumber q_D . The horizontal line indicates the BP frequency ω_{BP} . The black curve shows the linear dispersion $\omega = c_T q$, where c_T is the transverse sound speed, corresponding to phonon excitations. The green curve indicates $q_T(\omega)$, used to separate $g_T(\omega)$ into the phononic component $g_{\text{Ph}}(\omega)$ and the non-phononic component $g_{\text{Nph}}(\omega)$ in Eq. (24).

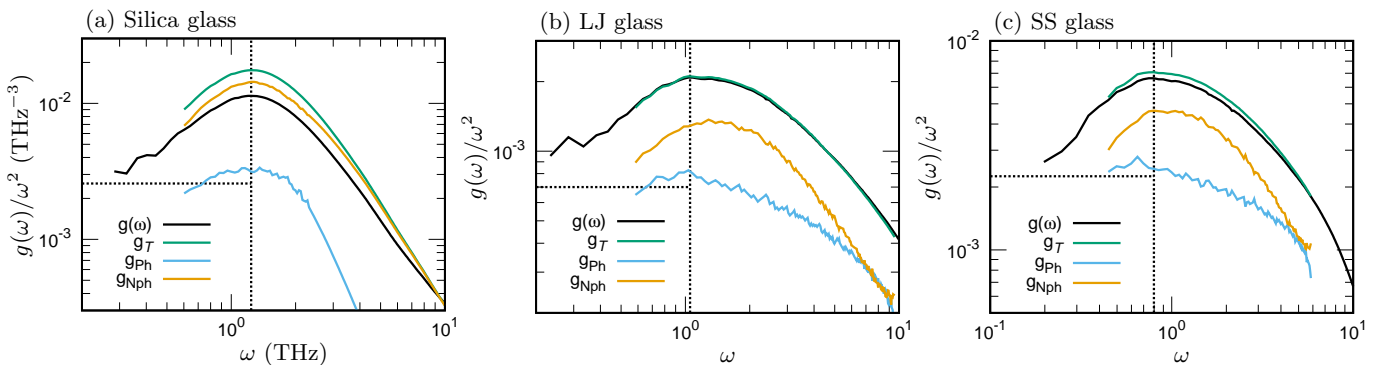


FIG. 5. Phononic and non-phononic components of the vibrational density of states. (a) Silica glass, (b) LJ glass, and (c) SS glass. The reduced vDOS $g(\omega)/\omega^2$ (black) is plotted as a function of the angular frequency ω , together with the transverse contribution $g_T(\omega)/\omega^2$ (green), obtained by integrating $S_T(q, \omega)$ over $0 \leq q \leq q_D$ according to Eq. (23). We further decompose $g_T(\omega)/\omega^2$ into its phononic and non-phononic components, $g_{\text{Ph}}(\omega)/\omega^2$ (cyan) and $g_{\text{Nph}}(\omega)/\omega^2$ (orange), as defined in Eq. (24). The vertical and horizontal dotted lines mark the BP frequency ω_{BP} and the Debye level A_D , respectively.

non-phononic excitations, as described below. As shown above, the transverse sector provides the dominant contribution in the BP regime, and we therefore focus on $S_T(q, \omega)$ and $g_T(\omega)$.

Figure 4 presents the transverse dynamical structure factor $S_T(q, \omega)$ in the low- q and low- ω regime. As reported in our recent work [83], silica, LJ, and SS glasses all exhibit, in addition to the phonon branch, a broad and nearly dispersionless excitation band in the BP-frequency regime that persists up to the Debye wavenumber q_D . Moreover, Mahajan *et al.* [84] recently compiled existing experimental and simulation data and concluded that such dispersionless-band excitations occur across a wide variety of amorphous systems. These observations suggest that the broad dispersionless band is a generic feature of amorphous solids and glasses.

We therefore separate the vDOS into the phonon-branch contribution and the contribution from the

broad dispersionless (non-phononic) band. For each frequency ω , we introduce a crossover wavenumber $q = q_T(\omega)$ in $S_T(q, \omega)$ that separates the phonon-branch-dominated regime ($q < q_T(\omega)$) from the dispersionless-band-dominated regime ($q > q_T(\omega)$). We then define the phononic and non-phononic contributions, $g_{\text{Ph}}(\omega)$ and $g_{\text{Nph}}(\omega)$, by

$$\begin{aligned} \frac{g_{\text{Ph}}(\omega)}{\omega^2} &= \frac{2M(\omega)}{q_D^3} \int_0^{q_T(\omega)} \frac{S_T(q, \omega)}{k_B T} dq, \\ \frac{g_{\text{Nph}}(\omega)}{\omega^2} &= \frac{2M(\omega)}{q_D^3} \int_{q_T(\omega)}^{q_D} \frac{S_T(q, \omega)}{k_B T} dq. \end{aligned} \quad (24)$$

By construction, the transverse contribution satisfies $g_T(\omega) = g_{\text{Ph}}(\omega) + g_{\text{Nph}}(\omega)$. The crossover wavenumber $q_T(\omega)$ is determined by analyzing $S_T(q, \omega)$ as a function of q at fixed ω . Details of the procedure are given in Sec. III D 3. The resulting $q_T(\omega)$ is shown as the green

curve in Fig. 4. As can be seen from the figure, this criterion provides a reasonable boundary separating the phonon branch from the broad dispersionless band.

Figure 5 shows the resulting decomposition into $g_{\text{Ph}}(\omega)$ and $g_{\text{Nph}}(\omega)$. For all three glasses, the decomposition demonstrates quantitatively that, in the BP-frequency regime, the vDOS contains mixed contributions from phononic and non-phononic excitations. The phononic component $g_{\text{Ph}}(\omega)$ approximately follows the Debye form $A_D\omega^2$, as expected. In addition, glasses exhibit a non-phononic component $g_{\text{Nph}}(\omega)$, which constitutes the excess modes over the Debye prediction and thus underlies the BP anomaly. These results provide direct, quantitative evidence that the broad band observed in the dynamical structure factor corresponds to non-phononic excitations and is the microscopic origin of the excess vDOS and the BP in both network-type and packing-type glasses.

E. Effective medium theory

Finally, we show that our simulation results are fully consistent with the predictions of the EMT for random spring networks [40, 42], which provides a theoretical basis for interpreting the broad band and the BP in terms of isostaticity and marginal stability [83]. We perform an EMT analysis following Refs. [40, 42], in which particles (nodes) are connected by linear springs to form a random spring network. Two control parameters govern mechanical stability: the connectivity (coordination number) z and the level of pre-stress $e > 0$, which quantifies the internal forces carried by the springs. Mechanical stability requires z to exceed the isostatic threshold $z_c = 2d$ in d dimensions, *i.e.*, a positive excess coordination $\delta z = z - z_c > 0$. In addition, if the pre-stress exceeds a critical value $e_c > 0$, the network becomes unstable; thus stability requires $e < e_c$. Within the EMT approximation, the random spring network is characterized by a complex, frequency-dependent effective spring constant $k_{\text{eff}}(\omega)$ (see Refs. [40, 42] for derivations and the full formulation), from which both the vDOS $g(\omega)$ and the dynamical structure factor $S(q, \omega)$ can be computed, as detailed below.

Given $k_{\text{eff}}(\omega)$, the vDOS and dynamical structure factor are obtained as

$$g(\omega) = \frac{2m\omega}{\pi} \text{Im} \left[\frac{3}{q_D^3} \int_0^{q_D} \frac{q^2 dq}{k_{\text{eff}}(\omega) q^2 - m\omega^2} \right], \quad (25)$$

$$S(q, \omega) = \frac{k_B T}{\pi} \frac{q^2}{\omega} \text{Im} \left[\frac{1}{k_{\text{eff}}(\omega) q^2 - m\omega^2} \right], \quad (26)$$

where Im denotes the imaginary part. Because transverse and longitudinal polarizations are not distinguished in this EMT, one has $S(q, \omega) = S_L(q, \omega) = S_T(q, \omega)/2$. Combining these expressions yields

$$\frac{g(\omega)}{\omega^2} = \frac{2m}{q_D^3} \int_0^{q_D} 3 \frac{S(q, \omega)}{k_B T} dq, \quad (27)$$

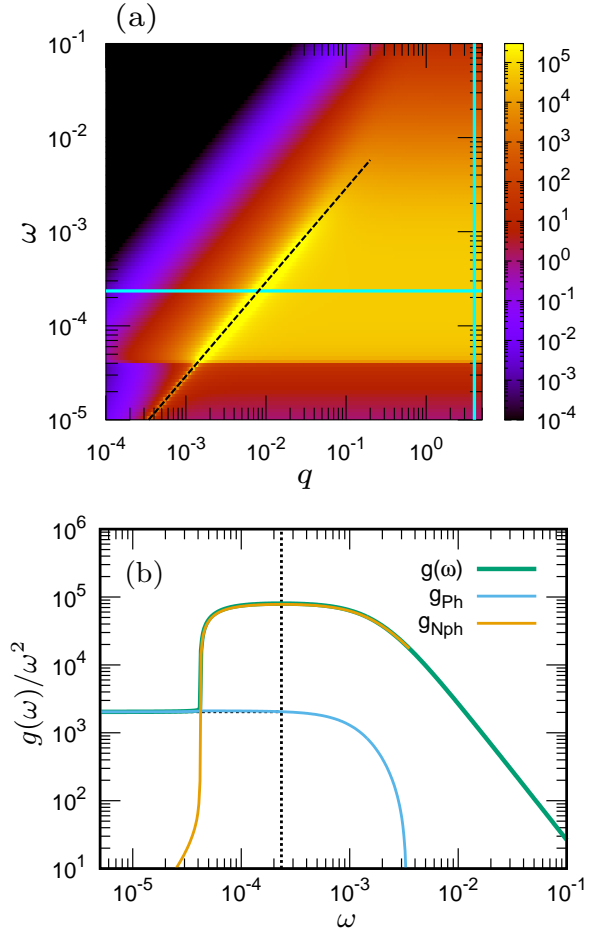


FIG. 6. Predictions of the EMT for random spring networks. (a) The dynamical structure factor $S(q, \omega)/(k_B T)$ [Eq. (26)] plotted as a function of wavenumber q and frequency ω . (b) The reduced vDOS $g(\omega)/\omega^2$ [Eq. (25)] plotted as a function of ω , together with its phononic and non-phononic components, $g_{\text{Ph}}(\omega)/\omega^2$ and $g_{\text{Nph}}(\omega)/\omega^2$, calculated from Eq. (28). In panel (a), the vertical line marks the Debye wavenumber q_D , and the horizontal line indicates the BP frequency ω_{BP} . The black dashed curve shows the linear dispersion $\omega = cq$, where c is the sound speed, corresponding to phonon excitations. In panel (b), the vertical and horizontal dotted lines indicate ω_{BP} and the Debye level A_D , respectively.

which corresponds to Eq. (23) upon identifying $3S \rightarrow S_T + S_L$ (sum over two transverse and one longitudinal polarizations) and, for identical particles in EMT, m with the effective mass $M(\omega)$. In what follows, we set $q_D = 4$ (dimensionless EMT units) and $m = 1$.

To capture the BP phenomenology observed in our simulations, we choose $\delta z = z - z_c = 10^{-2}$ and $e = e_c(1 - 5 \times 10^{-4})$, placing the network close to both isostaticity ($\delta z \ll 1$) and marginal stability ($e \lesssim e_c$). Figure 6(a) shows the resulting dynamical structure factor $S(q, \omega)/(k_B T)$. The spectrum exhibits phonon-like excitations with an approximately linear dispersion $\omega = cq$, where c is the sound speed. In addition, a broad, nearly wavenumber-independent (dispersionless) non-phononic

band emerges around the BP regime, in direct analogy with the simulation results.

Figure 6(b) presents the phononic and non-phononic contributions to the vDOS, $g_{\text{Ph}}(\omega)$ and $g_{\text{Nph}}(\omega)$. Within EMT, these components are expressed in terms of $k_{\text{eff}}(\omega)$ as

$$\begin{aligned} g_{\text{Ph}}(\omega) &= \frac{2m\omega^2}{\pi} \frac{3\pi}{2q_D^3} \text{Re} \left[\frac{1}{k_{\text{eff}}(\omega)^{3/2}} \right], \\ g_{\text{Nph}}(\omega) &= \frac{2m\omega}{\pi} \frac{3}{q_D^2} \text{Im} \left[\frac{1}{k_{\text{eff}}(\omega)} \right], \end{aligned} \quad (28)$$

where Re denotes the real part. The phononic component $g_{\text{Ph}}(\omega)$ approximately follows the Debye form $A_D\omega^2$, as expected, whereas the non-phononic component $g_{\text{Nph}}(\omega)$ provides the excess modes over the Debye prediction and thus underlies the BP anomaly.

Taken together, the EMT predictions reproduce the same phenomenology as our simulations: a broad dispersionless band in $S(q, \omega)$ and a corresponding excess contribution $g_{\text{Nph}}(\omega)$ that generates the BP. This consistency supports a unified scenario in which the dispersionless band and the BP originate from the proximity of glasses to isostaticity and marginal stability. Indeed, in our recent work [83], we demonstrated with more detailed simulation analyses that the BP in glasses can be rationalized within an isostaticity–marginal-stability framework.

V. CONCLUSIONS

In this study, we investigated BP anomalies in both a network-type glass (silica) and packing-type glasses (LJ and SS) by quantifying the vDOS from the dynamical structure factor using two complementary routes. In the first route, we assume incoherent scattering and extract the vDOS from the high-wavenumber data of longitudinal $S_L(q, \omega)$ [33–36]. We verified that this procedure reproduces the exact vDOS over the entire frequency range. Because scattering experiments predominantly access the longitudinal channel $S_L(q, \omega)$ [74], this route provides a practical experimental pathway to accurately determine the vDOS, including the BP.

In the second route, we quantify the vDOS by integrating the dynamical structure factors over low wavenumbers from 0 up to the Debye wavenumber [39–44]. Its key advantage is that it enables a quantitative decomposition of the vDOS into transverse and longitudinal sectors and, more importantly, into distinct wavenumber ranges. Using this decomposition, we found that the BP is predominantly governed by transverse vibrational states in all glasses studied here (silica, LJ, and SS), irrespective of

whether they are network-type or packing-type. Furthermore, by exploiting the wavenumber resolution, we separated the vDOS into phononic and non-phononic parts. We demonstrated quantitatively that, in the BP regime, the phononic contribution remains close to the Debye level, while an additional non-phononic contribution associated with the dispersionless excitation band builds up on top of it, thereby forming the BP anomaly.

While these conclusions hold universally across both network- and packing-type glasses, important differences also emerge between silica and the packing-dominated glasses. In silica glass, the tetrahedral network breaks local centrosymmetry, which gives rise to strong non-affine responses in both shear and bulk deformations [75–78]. Consistent with this elastic behavior, the transverse and longitudinal dynamical structure factors are more strongly coupled in silica, and $S_L(q, \omega)$ exhibits a q - ω dependence qualitatively similar to that of $S_T(q, \omega)$. As a result, insights obtained from the transverse channel can be more directly carried over to the longitudinal channel in silica glass. From an experimental standpoint, this is a particularly important advantage, because scattering measurements typically provide access to the longitudinal component [74].

Finally, our simulation results are fully consistent with the effective-medium theory for random spring networks [40, 42]. This agreement indicates that both the BP and the dispersionless excitation band can be understood within a unified framework based on isostaticity and marginal stability [83]. Building on these insights, a systematic re-examination of existing experimental and simulation datasets should further strengthen the present scenario and clarify its broader applicability [84].

ACKNOWLEDGMENTS

We thank Tatsuya Mori and Maiko Kofu for useful discussions. This work was supported by JSPS KAKENHI Grant Nos. 23H04495 and 25H01519, JST FOREST Grant No. JPMJFR236Q, and JST ERATO Grant No. JPMJER2401.

AUTHOR CONTRIBUTIONS STATEMENT

H.M. designed the research, analyzed the data, and wrote the paper. H.M and E.M. performed the research.

AUTHOR DECLARATIONS

The authors declare no conflicts of interest.

[1] M. A. Ramos, *Low-Temperature Thermal and Vibrational Properties of Disordered Solids: A Half-Century of Uni-*

versal “Anomalies” of Glasses (World Scientific Pub Co

- Inc, 2022).
- [2] T. Nakayama, Reports on Progress in Physics **65**, 1195 (2002).
 - [3] D. Kaya, N. L. Green, C. E. Maloney, and M. F. Islam, Science **329**, 656 (2010).
 - [4] C. Brito, O. Dauchot, G. Biroli, and J.-P. Bouchaud, Soft Matter **6**, 3013 (2010).
 - [5] S. Henkes, C. Brito, and O. Dauchot, Soft Matter **8**, 6092 (2012).
 - [6] H. Mizuno and A. Ikeda, Computational Simulations of the Vibrational Properties of Glasses, in *Low-Temperature Thermal and Vibrational Properties of Disordered Solids*, edited by M. A. Ramos (WORLD SCIENTIFIC (EUROPE), 2022) Chap. 10, pp. 375–433.
 - [7] K. Chen, W. G. Ellenbroek, Z. Zhang, D. T. N. Chen, P. J. Yunker, S. Henkes, C. Brito, O. Dauchot, W. van Saarloos, A. J. Liu, and A. G. Yodh, Phys. Rev. Lett. **105**, 025501 (2010).
 - [8] P. Tan, N. Xu, A. B. Schofield, and L. Xu, Phys. Rev. Lett. **108**, 095501 (2012).
 - [9] U. Buchenau, M. Prager, N. Nücker, A. J. Dianoux, N. Ahmad, and W. A. Phillips, Phys. Rev. B **34**, 5665 (1986).
 - [10] O. Yamamuro, T. Matsuo, K. Takeda, T. Kanaya, T. Kawaguchi, and K. Kaji, The Journal of Chemical Physics **105**, 732 (1996).
 - [11] M. Arai, Y. Inamura, T. Otomo, N. Kitamura, S. M. Bennington, and A. C. Hannon, Physica B: Condensed Matter **263-264**, 268 (1999).
 - [12] M. J. Harris, M. T. Dove, and J. M. Parker, Mineralogical Magazine **64**, 435–440 (2000).
 - [13] A. Monaco, A. I. Chumakov, G. Monaco, W. A. Crichton, A. Meyer, L. Comez, D. Fioretto, J. Korecki, and R. Rüffer, Phys. Rev. Lett. **97**, 135501 (2006).
 - [14] K. Niss, B. Begen, B. Frick, J. Ollivier, A. Beraud, A. Sokolov, V. N. Novikov, and C. Alba-Simionesco, Phys. Rev. Lett. **99**, 055502 (2007).
 - [15] B. Rufflé, D. A. Parshin, E. Courtens, and R. Vacher, Phys. Rev. Lett. **100**, 015501 (2008).
 - [16] G. Baldi, V. M. Giordano, G. Monaco, F. Sette, E. Fabiani, A. Fontana, and G. Ruocco, Phys. Rev. B **77**, 214309 (2008).
 - [17] G. Monaco and V. M. Giordano, Proc. Natl. Acad. Sci. USA **106**, 3659 (2009).
 - [18] G. Baldi, V. M. Giordano, G. Monaco, and B. Ruta, Phys. Rev. Lett. **104**, 195501 (2010).
 - [19] G. Baldi, V. M. Giordano, and G. Monaco, Phys. Rev. B **83**, 174203 (2011).
 - [20] B. Ruta, G. Baldi, F. Scarponi, D. Fioretto, V. M. Giordano, and G. Monaco, The Journal of Chemical Physics **137**, 214502 (2012).
 - [21] G. Baldi, M. Zanatta, E. Gilioli, V. Milman, K. Refson, B. Wehinger, B. Winkler, A. Fontana, and G. Monaco, Phys. Rev. Lett. **110**, 185503 (2013).
 - [22] A. I. Chumakov, G. Monaco, A. Fontana, A. Bosak, R. P. Hermann, D. Bessas, B. Wehinger, W. A. Crichton, M. Krisch, R. Rüffer, G. Baldi, G. Carini Jr., G. Carini, G. D’Angelo, E. Gilioli, G. Tripodo, M. Zanatta, B. Winkler, V. Milman, K. Refson, M. T. Dove, N. Dubrovinskaya, L. Dubrovinsky, R. Keding, and Y. Z. Yue, Phys. Rev. Lett. **112**, 025502 (2014).
 - [23] G. Baldi, V. M. Giordano, B. Ruta, and G. Monaco, Phys. Rev. B **93**, 144204 (2016).
 - [24] R. Shuker and R. W. Gammon, Phys. Rev. Lett. **25**, 222 (1970).
 - [25] N. V. Surovtsev and A. P. Sokolov, Phys. Rev. B **66**, 054205 (2002).
 - [26] B. Schmid and W. Schirmacher, Phys. Rev. Lett. **100**, 137402 (2008).
 - [27] U. Strom and P. C. Taylor, Phys. Rev. B **16**, 5512 (1977).
 - [28] T. Ohsaka and S. Oshikawa, Phys. Rev. B **57**, 4995 (1998).
 - [29] S. N. Taraskin, S. I. Simdyankin, S. R. Elliott, J. R. Neilson, and T. Lo, Phys. Rev. Lett. **97**, 055504 (2006).
 - [30] M. Kabeya, T. Mori, Y. Fujii, A. Koreeda, B. W. Lee, J.-H. Ko, and S. Kojima, Phys. Rev. B **94**, 224204 (2016).
 - [31] T. Mori, Y. Jiang, Y. Fujii, S. Kitani, H. Mizuno, A. Koreeda, L. Motoji, H. Tokoro, K. Shiraki, Y. Yamamoto, and S. Kojima, Phys. Rev. E **102**, 022502 (2020).
 - [32] D. Kyotani, S. H. Oh, S. Kitani, Y. Fujii, H. Hijya, H. Mizuno, S. Kohara, A. Koreeda, A. Masuno, H. Kawaji, S. Kojima, Y. Yamamoto, and T. Mori, Scientific Reports **15**, 9617 (2025).
 - [33] D. L. Price and J. M. Carpenter, Journal of Non-Crystalline Solids **92**, 153 (1987).
 - [34] A. Pasquarello, J. Sarnthein, and R. Car, Phys. Rev. B **57**, 14133 (1998).
 - [35] B. Fultz, Progress in Materials Science **55**, 247 (2010).
 - [36] G. L. Squires, *Introduction to the Theory of Thermal Neutron Scattering*, 3rd ed. (Cambridge University Press, 2012).
 - [37] G. S. Grest, S. R. Nagel, A. Rahman, and J. Witten, T. A., The Journal of Chemical Physics **74**, 3532 (1981).
 - [38] A. Ikeda, L. Berthier, and G. Biroli, The Journal of Chemical Physics **138**, 12A507 (2013).
 - [39] W. Schirmacher, Europhys. Lett. **73**, 892 (2006).
 - [40] M. Wyart, EPL (Europhysics Letters) **89**, 64001 (2010).
 - [41] A. Marruzzo, W. Schirmacher, A. Fratallocchi, and G. Ruocco, Scientific Reports **3**, 1407 (2013).
 - [42] E. DeGiuli, A. Laversanne-Finot, G. Düring, E. Lerner, and M. Wyart, Soft Matter **10**, 5628 (2014).
 - [43] W. Schirmacher, T. Scopigno, and G. Ruocco, Journal of Non-Crystalline Solids **407**, 133 (2015).
 - [44] H. Mizuno and A. Ikeda, Phys. Rev. E **98**, 062612 (2018).
 - [45] B. W. H. van Beest, G. J. Kramer, and R. A. van Santen, Phys. Rev. Lett. **64**, 1955 (1990).
 - [46] D. Wolf, Phys. Rev. Lett. **68**, 3315 (1992).
 - [47] D. Wolf, P. Keblinski, S. R. Phillpot, and J. Eggebrecht, The Journal of Chemical Physics **110**, 8254 (1999).
 - [48] A. Carré, L. Berthier, J. Horbach, S. Ispas, and W. Kob, The Journal of Chemical Physics **127**, 114512 (2007).
 - [49] A. Carré, S. Ispas, J. Horbach, and W. Kob, Computational Materials Science **124**, 323 (2016).
 - [50] S. Sundararaman, L. Huang, S. Ispas, and W. Kob, The Journal of Chemical Physics **148**, 194504 (2018).
 - [51] B. Mantisi, A. Tanguy, G. Kermouche, and E. Barthel, The European Physical Journal B **85**, 304 (2012).
 - [52] N. S. Shcheblanov, B. Mantisi, P. Umari, and A. Tanguy, Journal of Non-Crystalline Solids **428**, 6 (2015).
 - [53] T. Damart, A. Tanguy, and D. Rodney, Phys. Rev. B **95**, 054203 (2017).
 - [54] A. El Hamdaoui, E. M. Ghardi, M. J. D. Rushton, A. Hasnaoui, and S. Ouaskit, Journal of the American Ceramic Society **108**, e20631 (2025).
 - [55] P. Vashishta, R. K. Kalia, J. P. Rino, and I. Ebbsjö, Physical Review B **41**, 12197 (1990).

- [56] S. Plimpton, *Journal of Computational Physics* **117**, 1 (1995).
- [57] S. Nosé, *The Journal of Chemical Physics* **81**, 511 (1984).
- [58] W. G. Hoover, *Physical Review A* **31**, 1695 (1985).
- [59] G. Monaco and S. Mossa, *Proceedings of the National Academy of Sciences* **106**, 16907 (2009).
- [60] H. Mizuno, S. Mossa, and J.-L. Barrat, *Phys. Rev. E* **87**, 042306 (2013).
- [61] M. Shimada, H. Mizuno, and A. Ikeda, *Phys. Rev. E* **97**, 022609 (2018).
- [62] H. Mizuno, L. E. Silbert, M. Sperl, S. Mossa, and J.-L. Barrat, *Phys. Rev. E* **93**, 043314 (2016).
- [63] H. Mizuno, S. Mossa, and J.-L. Barrat, *EPL (Europhysics Letters)* **104**, 56001 (2013).
- [64] H. Mizuno, S. Mossa, and J.-L. Barrat, *Proceedings of the National Academy of Sciences* **111**, 11949 (2014).
- [65] H. Mizuno, S. Mossa, and J.-L. Barrat, *Phys. Rev. B* **94**, 144303 (2016).
- [66] H. Mizuno, H. Shiba, and A. Ikeda, *Proceedings of the National Academy of Sciences* **114**, E9767 (2017).
- [67] N. W. Ashcroft and N. D. Mermin, *Solid State Physics* (Harcourt College Publishers, New York, 1976).
- [68] A. Lemaitre and C. Maloney, *Journal of Statistical Physics* **123**, 415 (2006).
- [69] H. Mizuno, K. Saitoh, and L. E. Silbert, *Phys. Rev. E* **93**, 062905 (2016).
- [70] A. Zaccone and E. Scossa-Romano, *Phys. Rev. B* **83**, 184205 (2011).
- [71] G. N. Greaves, A. L. Greer, R. S. Lakes, and T. Rouxel, *Nature Materials* **10**, 823 (2011).
- [72] E. Duval, T. Deschamps, and L. Saviot, *The Journal of Chemical Physics* **139**, 064506 (2013).
- [73] G. S. Grest, S. R. Nagel, and A. Rahman, *Phys. Rev. Lett.* **49**, 1271 (1982).
- [74] J.-B. Suck, P. A. Egelstaff, R. A. Robinson, D. S. Sivia, and A. D. Taylor, *Europhysics Letters* **19**, 207 (1992).
- [75] R. Milkus and A. Zaccone, *Phys. Rev. B* **93**, 094204 (2016).
- [76] J. Krausser, R. Milkus, and A. Zaccone, *Soft Matter* **13**, 6079 (2017).
- [77] E. Minamitani, T. Nakamura, I. Obayashi, and H. Mizuno, *Nature Communications* **16**, 8226 (2025).
- [78] B. Cui, A. Zaccone, and D. Rodney, *The Journal of Chemical Physics* **151**, 224509 (2019).
- [79] In the second, wavenumber-resolved approach based on Eq. (23), accurately estimating the low-frequency vDOS requires reliable data for the phonon-branch contribution in the low- q part of the dynamical structure factor. If the low- q phonon branch is not computed with sufficient accuracy, the q -integration in Eq. (23) becomes unreliable at small ω , making it difficult to obtain a quantitative estimate of $g_{T+L}(\omega)$ near the low-frequency edge. For this reason, in Fig. 3 we do not display the data at the lowest frequencies, where the vDOS estimate from the second route is not sufficiently controlled.
- [80] Y. M. Beltukov, C. Fusco, D. A. Parshin, and A. Tanguy, *Phys. Rev. E* **93**, 023006 (2016).
- [81] Y. M. Beltukov, D. A. Parshin, V. M. Giordano, and A. Tanguy, *Phys. Rev. E* **98**, 023005 (2018).
- [82] E. Minamitani, T. Shiga, M. Kashiwagi, and I. Obayashi, *The Journal of Chemical Physics* **156**, 244502 (2022).
- [83] H. Mizuno, T. Mori, G. Baldi, and E. Minamitani, *Boson peak in covalent network glasses: Isostaticity and marginal stability* (2025), arXiv:2508.20481v1 (cond-mat.dis-nn; cond-mat.soft), submitted 28 Aug 2025, arXiv:2508.20481 [cond-mat.dis-nn].
- [84] S. Mahajan, L.-Z. Huang, C. Jiang, Y.-J. Wang, M. P. Ciamarra, J. Zhang, and M. Baggioli, *A flat-mode perspective on the boson peak in amorphous solids* (2025), arXiv:2509.06340 [cond-mat.soft].